

Supplemental Material to *Dynamical Quantum Phase Transitions in Spin Chains with Long-Range Interactions: Merging different concepts of non-equilibrium criticality*

Bojan Žunkovič,¹ Markus Heyl,^{2,3} Michael Knap,² and Alessandro Silva¹

¹*SISSA — International School for Advanced Studies, via Bonomea 265, 34136 Trieste, Italy*

²*Department of Physics, Walter Schottky Institute, and Institute for Advanced Study, Technical University of Munich, 85748 Garching, Germany*

³*Max-Planck-Institut für Physik komplexer Systeme, 01187 Dresden, Germany*

In this supplement we provide further supporting material including more details on the dynamical properties of the long-range transverse-field Ising models as well as on our numerical approach.

I. INFINITE-RANGE TRANSVERSE-FIELD ISING MODEL

In this section we summarize both equilibrium and nonequilibrium properties of the infinite-range transverse-field Ising model described by the Hamiltonian

$$H = -\frac{J}{N} \sum_{j,k=1}^N \sigma_j^x \sigma_k^x - h \sum_j^N \sigma_j^z, \quad (1)$$

where σ_i^α are Pauli matrices satisfying the commutation relations $[\sigma_j^\alpha, \sigma_j^\beta] = 2i\epsilon^{\alpha\beta\gamma}\sigma_j^\gamma$. After recapitulating the equilibrium properties of the model we describe two notions of dynamical phase transitions and their relation to the bifurcation of semiclassical trajectories. We end by discussing the distinctive nature of the dynamical transition compared to the finite temperature transition in the model.

A. Equilibrium phase diagram

The Hamiltonian Eq.(1) can be conveniently rewritten as $H/N = -J(S^x)^2 - hS^z$, with $S^a = \frac{1}{N} \sum_j \sigma_j^a$, ($a = x, y, z$), denoting the collective spin operators obeying the commutation relations $[S^x, S^y] = \frac{2i}{N} S^z$. At zero temperature the phase diagram is determined by the minima of the semi-classical energy function

$$H(\theta, \varphi) = -J \cos^2(\theta) \cos^2(\varphi) - h \sin(\theta), \quad (2)$$

where $(S^x, S^y, S^z) \rightarrow (\cos \theta \cos \varphi, \cos \theta \sin \varphi, \sin \theta)$. The minima of the energy (2) as a function of θ lie at $\theta = \arcsin(h/2J)$ (ferromagnetic phase) for $h/J < 2$ and at $\theta = \pi/2$ for $h/J > 2$ (paramagnetic phase). At finite temperature we resort to the mean-field analysis leading to the self-consistency equation

$$\sigma^x = \frac{2J\sigma^x}{\sqrt{h^2 + 4J^2(\sigma^x)^2}} \tanh\left(\frac{1}{T} \sqrt{h^2 + 4J^2(\sigma^x)^2}\right), \quad (3)$$

where $\sigma^a = \langle S^a \rangle$ for $a = x, y, z$. Equation (3) identifies two regions in the $(T/J, h/J)$ plane, a ferromagnetic one with $\sigma^x \neq 0$ and a paramagnetic one with $\sigma^x = 0$. The boundary is given by

$$\frac{h_c^{\text{th}}}{2J} = \tanh\left(\frac{h_c^{\text{th}}}{T}\right). \quad (4)$$

B. Dynamical phase transition

Let us now discuss the semiclassical picture of the dynamical transitions and compare it to the exact numerical results for large system sizes.

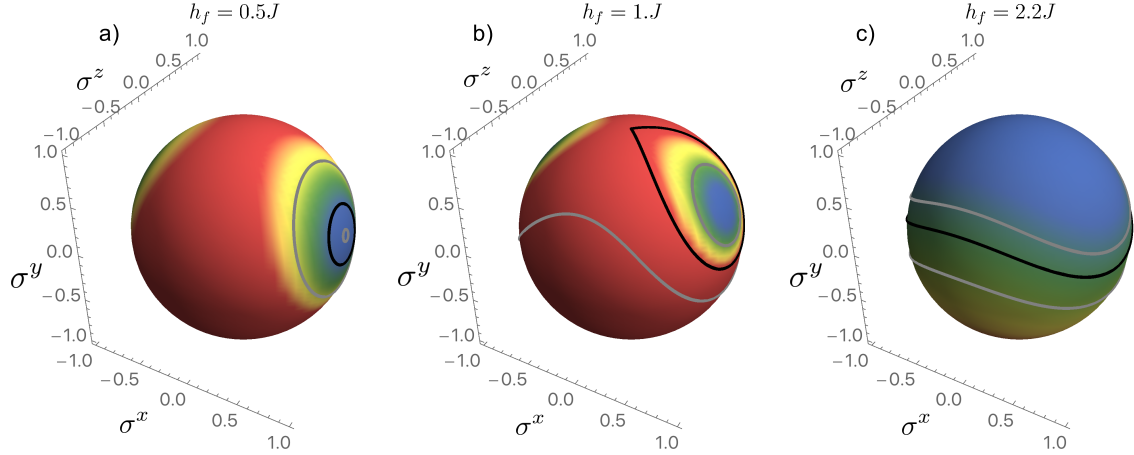


Figure 1: Phase space portraits of the energy function $H(\theta, \varphi)$, where the polar angle θ is measured from the xy plane and the azimuth φ from the x axis. The energy is displayed by color – we use warm colors for high energy and cold colors for low energy. The black lines show trajectories for the quench from $h_i = 0$, the gray lines correspond to initial states with a bit higher and lower initial energy with respect to the final Hamiltonian.

1. Semiclassical analysis

In the large- N limit the mean-field picture provides the correct dynamical behavior of local observables. Starting from a semiclassical state (for example a ground state at some h_i), where all spins are pointing in one direction determined by two angles θ_i and φ_i , all spins evolve according to the semiclassical equations and therefore keep pointing in the same direction. In this situation the state can be described as a single large spin, the dynamics of which can conveniently be visualized on the Bloch sphere (see Figure 1).

When quenching from the ferromagnetic phase, $h_i < 2$, we observe two types of trajectories, which can be characterized by the time-averaged magnetization $\overline{\sigma^x}$.^{1,2} Trajectories of the first type occur for small enough h_f and are restricted to a single hemisphere giving rise to a non-vanishing magnetization $\overline{\sigma^x}$. Trajectories of the second type occur for large h_f and are symmetric under the transformation $x \rightarrow -x$ with a vanishing time-averaged magnetization $\overline{\sigma^x}$. The critical magnetic field separating these two regions can be calculated from the condition $H_f(\theta_i, \varphi_i) = H_f(\pi/2, 0)$ and is given by $h_c = J + h_i/2$.

The transition between the symmetric and symmetry-broken trajectories can also be captured by another notion of dynamical criticality^{3,4} consisting in the observation of singularities in time of the probability to return to the ground state manifold (in short return probability). For that purpose we need the overlap between two semiclassical states that is given by

$$\langle \theta_1, \varphi_1 | \theta_2, \varphi_2 \rangle = \left(\frac{1 + \vec{\sigma}_1 \cdot \vec{\sigma}_2}{2} \right)^N, \quad (5)$$

where $\vec{\sigma} = (\sigma^x, \sigma^y, \sigma^z)$. For our choice of initial condition of a fully polarized state, we thus directly obtain that $P_{\pm}(t) = \exp[-N\lambda_{\pm}(t)] = \left(\frac{1 \pm \sigma^x(t)}{2} \right)^N$. Cusps in the return probability $P(t) = P_-(t) + P_+(t)$ occur whenever $P_+(t_c) = P_-(t_c)$ defining the critical time t_c . This condition is equivalent to $\exp[-\lambda_+(t_c)] - \exp[-\lambda_-(t_c)] = \sigma^x = 0$. While the presence of cusps in the return probability is a signature of symmetric trajectories, the absence of cusps is a signature of symmetry-broken trajectories, with respect to the transformation $\sigma_x \rightarrow -\sigma_x$.

The physical meaning of the dynamical phase transition signaled either by the cusps in the return probability or the time-averaged order parameter $\overline{\sigma^x}$ can be understood from Figure 1, where we show different types of trajectories and the energy function in the semiclassical phase-space. If the transverse-field is larger than the zero temperature critical field ($h_f > 2$), we are in the paramagnetic phase where the ground state, the energy function and all trajectories are symmetric. Conversely, if $h_i, h_f < 2$ the phase space splits into a symmetry-broken part at low energies and a symmetric part at high energies. The time-averaged order parameter and the cusps in the return probability, indicate a bifurcation of the trajectories as we change the initial or the final Hamiltonian.

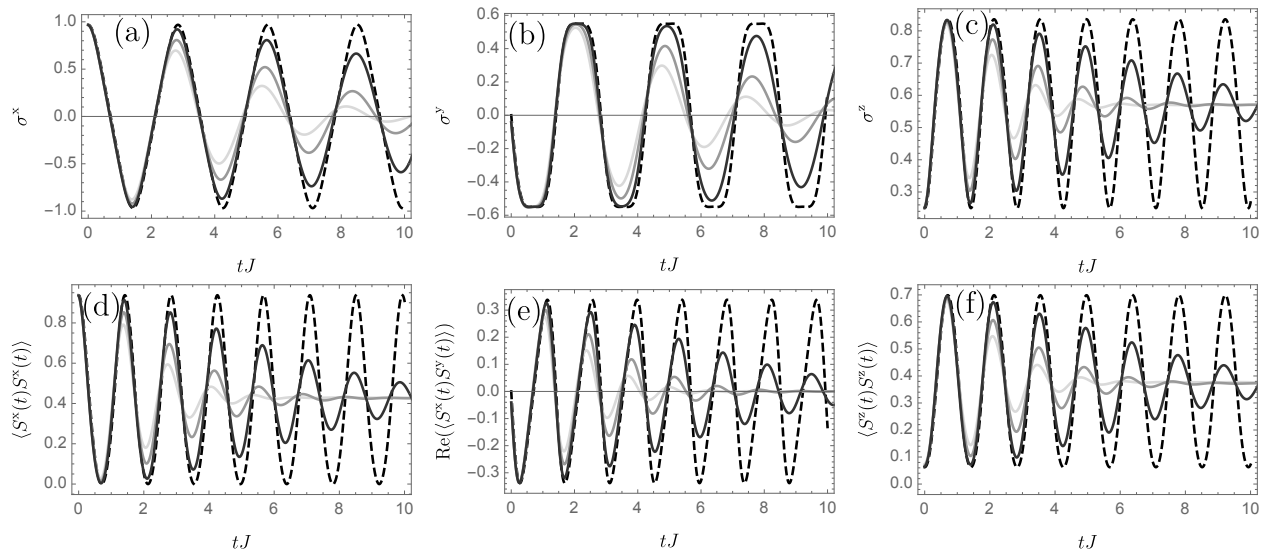


Figure 2: Convergence of local observables to the semiclassical values with the increasing system size $N = 100, 200, 800$ (from bright to dark): (a)-(c) on-site expectations, (d)-(f) two point correlations. The dashed line shows the semiclassical result. A quench from the ferromagnetic phase ($h_i = 0.5$) to the paramagnetic phase ($h_f = 1.6$) is presented.

2. Exact numerical results

The semiclassical formula Eq.(5) predicts correctly the cusps emerging in $P(t)$ whenever $P_+(t_c) = P_-(t_c)$ at a critical time t_c . However, also the individual contributions $P_+(t), P_-(t)$ can exhibit singularities in time. We find that these are correctly predicted by Eq. (5) only for $h_i = 0$ while for $h_i \neq 0$ semiclassics smoothens them artificially. It is important to note that these additional singularities are not observed in $P(t)$ in the thermodynamic limit which is therefore correctly described by the semiclassical formula. Let us discuss this point more in depth by performing a careful system size scaling of the model. To obtain exact results for finite size systems we diagonalize the Hamiltonian Eq. (1) in the spin $N/2$ subspace with the two degenerate ground states (with exponentially close energy as N increases). We first show that by increasing system size the exact trajectory of the magnetization converges to the semiclassical result (which we also find for higher moments; see Figure 2). In contrast to the local observables, the return probabilities and the Loschmidt echo approach the semiclassical result only partially as the system size is increased. The exact Loschmidt echo displays cusps at the minima of $\sigma^x(t)$ (for all system sizes), absent in the semiclassical description for quenches from $h_i > 0$. This is essentially due to the fact that the Loschmidt echo *is not* a local observable. However, singularities in $P(t)$ are correctly predicted by the semiclassical formula: this is shown in Figure 3 where the singularities in the Loschmidt echo align with the minima of the order parameter $\sigma^x(t)$, whereas the singularities of the return probability align with the zeros of the order parameter $\sigma^x(t)$.

C. Difference between dynamical and thermal phase transitions

In order to assess if there is any relation between the dynamical and the thermal phase transition in the infinite-range Ising model we compare the energy density of the critical trajectory governing the phase transition at some h_f with the energy density associated to the critical temperature at the same h_f . We start by writing the energy of the initial state (the ground state of the initial Hamiltonian corresponding to h_i) with respect to the final Hamiltonian

$$e(h_i, h_f) = \frac{-2h_f h_i + h_i^2 - 4J^2}{4J}. \quad (6)$$

At the critical field $h_f = h_c = J + h_i/2$ we obtain the energy density of the critical trajectory corresponding to the quench from h_i

$$e_1 = -J - \frac{h_i}{2}. \quad (7)$$

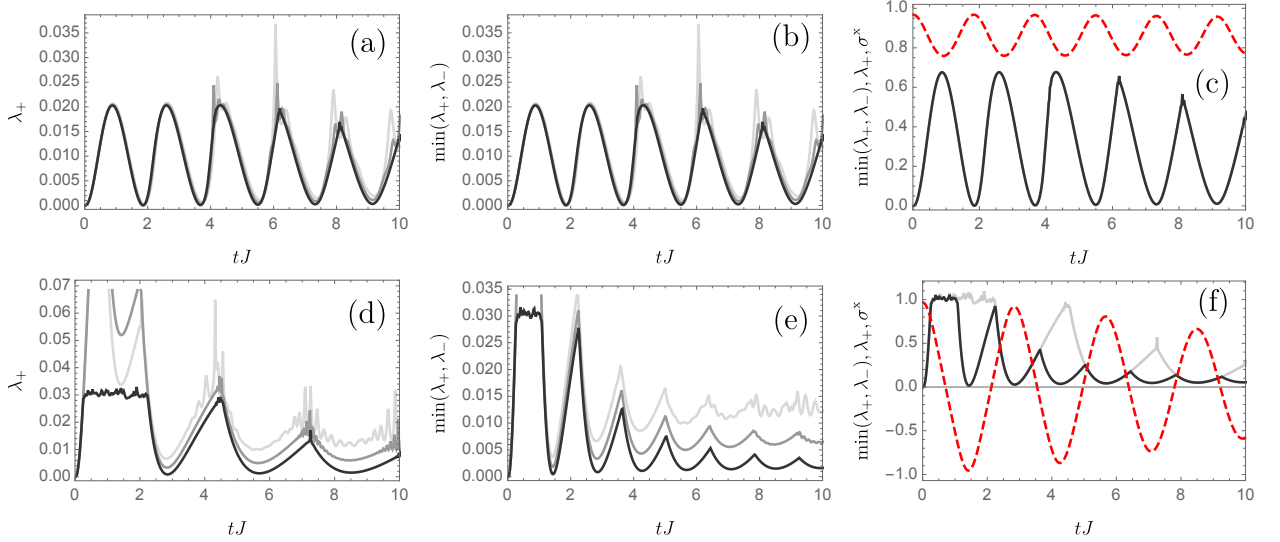


Figure 3: System size scaling of the Loschmidt echo (a,d) and the return probability (b,e) for a quenches from $h_i = 0$ to $h_f = 0.9$ (a,b,c) and $h_f = 1.6$ (d,e,f). If we stay on the ferromagnetic side the singularities that may appear for finite system sizes are smoothened with increasing system size. Conversely, for the quenches to the paramagnetic side ($h = 1.6$) the singularities become more pronounced as the system size is increased. Similarly for the return probability we observe singularities only for quenches across the dynamical critical point. In panels (c,f) we compare the rescaled Loashmidt echo (gray line) and the return probability (black line) with the time evolutions of the longitudinal magnetisation $\sigma^x(t)$ (red dashed line). We observe that as in the semiclassical case the singularities in the Loschmidt echo correspond to the minima of $\sigma^x(t)$, whereas the singularities in the return probability correspond zeros of $\sigma^x(t)$. Accordingly, the period of cusps in the Loschmidt echo is twice the period of the cusps in the return probability. System sizes: $N = 100, 200, 800$ from bright to dark (in panels a,b,d,e) and $N = 800$ (in panels c,f).

We compare this energy density with the one corresponding to the critical temperature at $h_f = h_c$. From the Eq.(4) we calculate the critical temperature $T_c(h_c) = h_c / \text{arctanh}(h_c/2J)$, which corresponds to the thermal energy density

$$e_2 = -\frac{h_c^2}{2J} = -\frac{(h_i + 2J)^2}{8J}. \quad (8)$$

From Figure 4 (a), where we plot both energy densities, we see that the energy density of the critical trajectory is strictly smaller than the thermal density. The final magnetic field at which the energy densities corresponding to the thermal and initial state coincide is

$$h_f(e_1 = e_2) = \frac{1}{2} \left(\sqrt{8J^2 - h_i^2} + h_i \right). \quad (9)$$

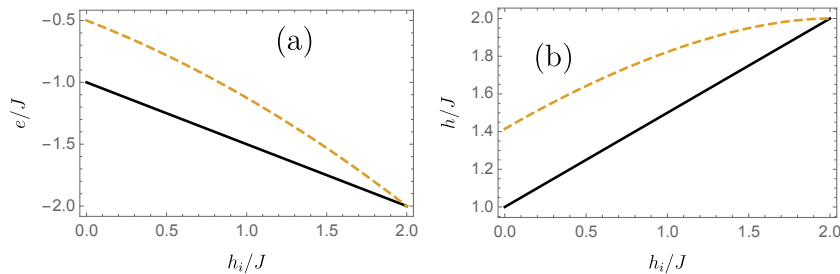


Figure 4: (a) Energy density of the quench e_1 (black line) and thermal energy density e_2 (orange dashed) as a function of the initial magnetic field. (b) The dynamical critical field (black line) and the field at which the energy densities of the thermal and the initial state coincides, equation (9), (orange dashed) as a function of the initial magnetic field. In both cases we see significant difference for small initial magnetic fields.

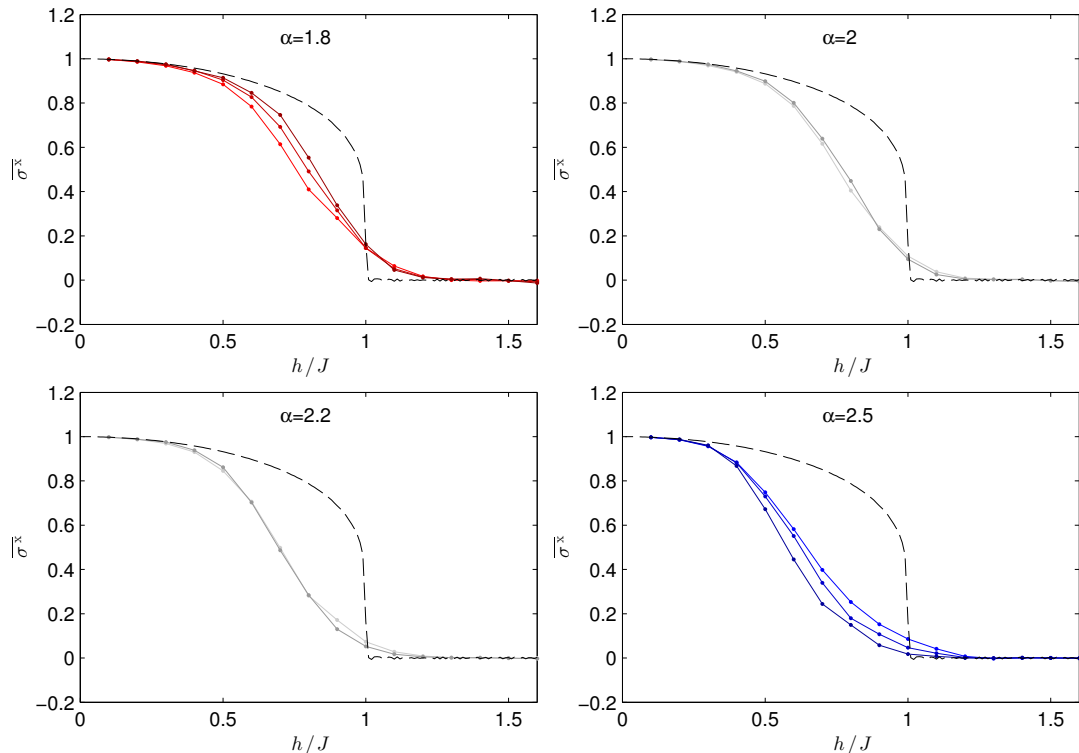


Figure 5: Scaling of the time-averaged order parameter $\overline{\sigma^x}$ with the system size. From bright to dark the colors correspond to increasing system sizes $N = 25, 50, 100$. The plot calculated for $\alpha = 1.8$ shows convergence of $\overline{\sigma^x}$ to non-vanishing values for $h < 1$, while the plot calculated for $\alpha = 2.5$ indicates decrease of $\overline{\sigma^x}$ with the system size for all h . The data for $\alpha = 2.0$ and $\alpha = 2.2$ is inconclusive due to the weak finite size flow.

In Figure 4 (b) we compare the dynamical critical field with equation (9) and observe that the field strength, at which the thermal energy density agrees with the energy density of the initial state, is significantly larger (for small h_i) as the dynamical critical value.

II. FINITE-RANGE INTERACTIONS $\alpha > 0$

We present additional numerical results for the finite-size flow of the time-averaged magnetization $\overline{\sigma^x}$, the cusps in the Loschmidt echo and the return probabilities in the case of finite interaction ranges. Finally, we discuss perturbative arguments for the absence of the phase transition at large interaction exponent α .

A. Time-averaged order parameter

We now focus on the scaling of the time-averaged order parameter with the system size. In Figure 5 we show the scaling of $\overline{\sigma^x}$ with the system size and for $\alpha = 1.8, 2, 2.2$ and 2.5 . For the first, $\alpha = 1.8$, we see an increase and for the last, $\alpha = 2.5$, a decrease of $\overline{\sigma^x}$ with the system size. This indicates that in the thermodynamic limit the order parameter stays finite up to some critical field in the former case whereas it vanishes for all values of the field in the latter case. While for $\alpha = 2$ and $\alpha = 2.2$ the finite-size flow is not conclusive at the achievable N , we can estimate the transition to the region $2 \lesssim \alpha \lesssim 2.4$.

B. Loschmidt echo and the return probability

In this section we study the scaling of the Loschmidt echo and the return probability with system size for nonzero $\alpha > 0$. As for the dynamical order parameter, the understanding of the behavior of these quantities developed in the

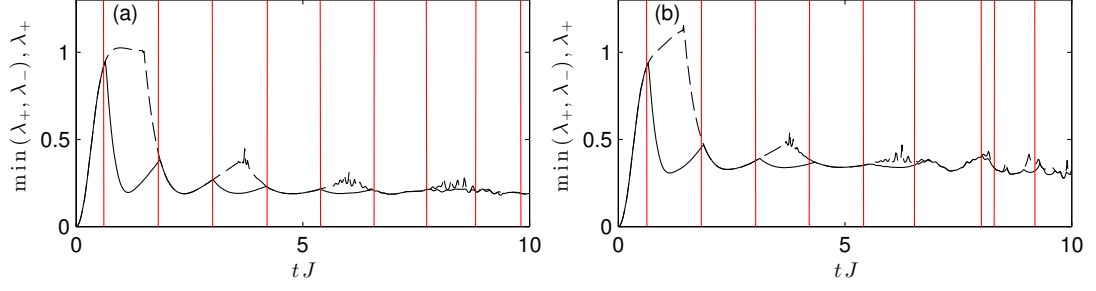


Figure 6: Position of the cusp singularities of the Loschmidt echo (dashed line) and the return probability (full line) compared to the zeros of the order parameter $\sigma^x(t)$ (vertical red lines). We show data for $\alpha = 1.8$ (a) and $\alpha = 2.5$ (b) and observe that the semiclassical picture remains valid also in the case of short range interactions $\alpha > 2$, where the time-averaged order parameter vanishes. The system size is $N = 100$.

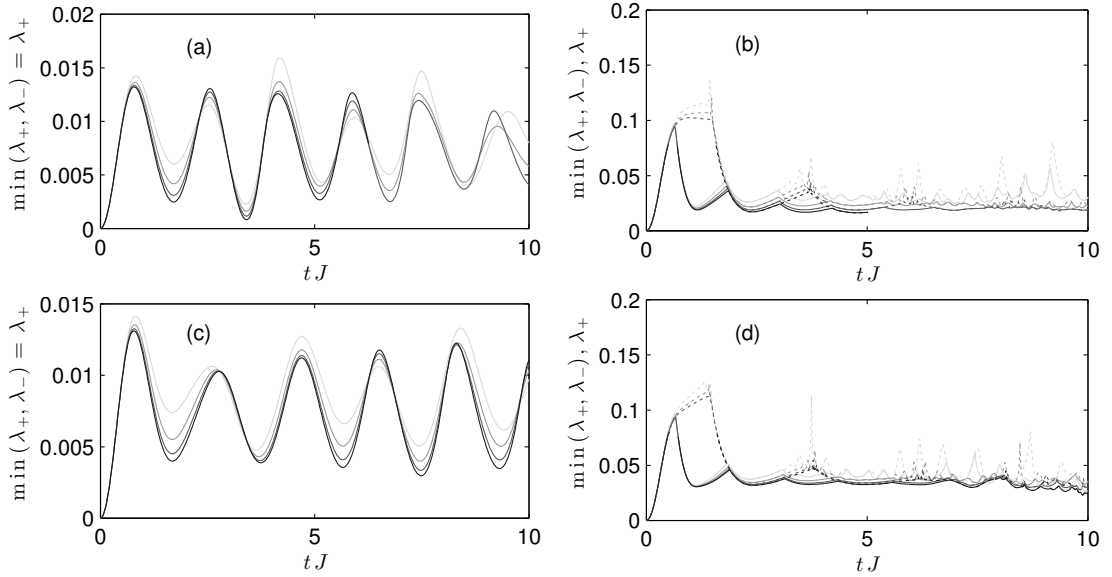


Figure 7: Scaling of the ground-state-manifold return rate $\min(\lambda_+(t), \lambda_-(t))$ (full lines) and the Loschmidt rate λ_+ (dotted lines) with the system size for quenches to $h_f = 0.5$ (a,c) and $h_f = 1.5$ (b,d). Panels (a,b) correspond to the interaction range $\alpha = 1.8$, where we still see a non-vanishing time-averaged order parameter. The panels (c,d) show simulations for $\alpha = 2.5$, where the time-averaged order parameter vanishes, but the cusp singularities in the return probability and Loschmidt rate still persist. Different system sizes, $N = 25, 50, 100, 200$, are indicated from bright to dark.

infinite-range case $\alpha = 0$ turns out to give us clear guidelines to interpret the data obtain numerically for finite α . For small α singularities in the Loschmidt echo coincide with local minima of $\sigma^x(t)$ and singularities in the return probability coincide with zeros of $\sigma^x(t)$ (see Figure 6). In contrast to the dynamical order parameter the singularities in the Loschmidt rate and the return probability persist for any value of α . For the system size dependence of these quantities see Figure 7.

In summary, for any value of α , the order parameter and the cusps in the return probability indicate a change in symmetry of the trajectory in phase space of the total magnetization of the system. For quenches below the critical point the magnetization precesses to its final value along the longitudinal direction and for quenches above the critical point it precesses around the transverse direction. While the presence or absence of a DQPT-OP depends strongly on α , the transition due to a change in symmetry of the trajectories is robust and occurs for any α .

We note that after our work has appeared, the Loschmidt echo has been calculated in Refs. 5–7, whereas the return probability to the ground state manifold has not been further studied in these works.

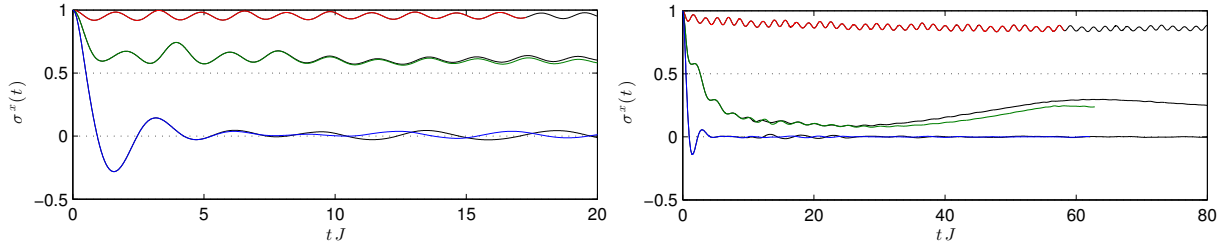


Figure 8: Convergence of $\sigma^x(t)$ for $\alpha = 1.8$ (left) and $\alpha = 2.5$ (right) with increasing matrix product state bond dimension – $D = 60$ (black lines) and $D = 100$ (colored lines). We show the data for $h_f=0.4$ (red), 0.8 (green), 1.2 (blue). The system size is 100.

C. Absence of a DQPT-OP for large α

Finally, let us provide a further analytical argument why the DQPT-OP disappears for large α as opposed to the claim recently put forward in Ref. 8. In Ref. 8, by an extrapolation of short-time data ($tJ < 10$) to infinitely late times, a finite order parameter has been predicted in a prethermal regime in our model for all values of α . In the following we provide an analytical argument based on a perturbative construction of the generalized Gibbs ensemble (GGE) describing the prethermal state for $\alpha \gg 1$ that this is impossible. At large but finite α we write

$$H = \frac{J}{N(\alpha)} \sum_{i,j} \frac{\sigma_i^z \sigma_j^z}{|i-j|^\alpha} + h \sum_i \sigma_i^x = H_I + V, \quad (10)$$

where

$$H_I = \frac{J}{N(\alpha)} \sum_i (\sigma_i^z \sigma_{i+1}^z + h.c.) + h \sum_i \sigma_i^x, \quad (11)$$

$$V = \frac{J}{N(\alpha)} \sum_{|i-j| \geq 2} \frac{1}{|i-j|^\alpha} \sigma_i^z \sigma_j^z. \quad (12)$$

Here, H_I is the Hamiltonian of the nearest-neighbor quantum Ising chain. For this model it has been shown that for any quantum quench of the transverse field the order parameter decays exponentially in time, implying absence of long-range order.⁹ This result can be obtained by computing the correlation function using the GGE

$$C(t) = \text{Tr}[\rho_{GGE} \sigma_{i+r}^z(t) \sigma_i^z(t)], \quad (13)$$

where $\rho_{GGE} \propto \exp[-\sum_n \lambda_n \hat{I}_n]$ and \hat{I}_n are the local constants of motion of the Ising chain.⁹ Let us now turn to the full Hamiltonian: when α is large, we have a quantum Ising chain with a perturbation V exponentially small in α . The prethermal state attained by this system for large α is still described by a GGE $\tilde{\rho}_{GGE} \propto \exp[-\sum_n \lambda_n \tilde{I}_n]$, where \tilde{I}_n are the “approximate” constants of motion obtained by $\tilde{I}_n = e^{-S} I_n e^S$, where e^S is the rotation that diagonalizes $H_I + V$ perturbatively in V .¹⁰ It is evident that since in the limit $\alpha \gg 1$ the new constants of motion \tilde{I}_n are essentially the old ones up to exponentially small corrections in α , the correlator Eq.(13) is expected to display the same behavior as in the short range case. This construction, ruling out long-range order for any quench in the limit of large α , contradicts the scenario in which the dynamical phase transition would survive for all α with a shifted critical field which has been proposed in Ref. 8.

It is important to stress that the GGE and the results on which the argument above is based are not perturbative in the transverse field h : a perturbative expansion in h would *always* lead to the conclusion of the presence of long-range order for small enough transverse field for all α , even for $\alpha = +\infty$. Since, however, the exact result for the correlation function gives $C(r, t \rightarrow +\infty) \propto e^{-r/\xi}$, where $\xi = h^2/4 + O(h^4)$, a straightforward perturbative expansion would not predict the destruction of long-range order.

The apparent contradiction with Ref. 8 might be explained by the fact that one cannot estimate the error of an infinite time extrapolation in an unbiased way without knowing the functional form or at least the time scales of the function.

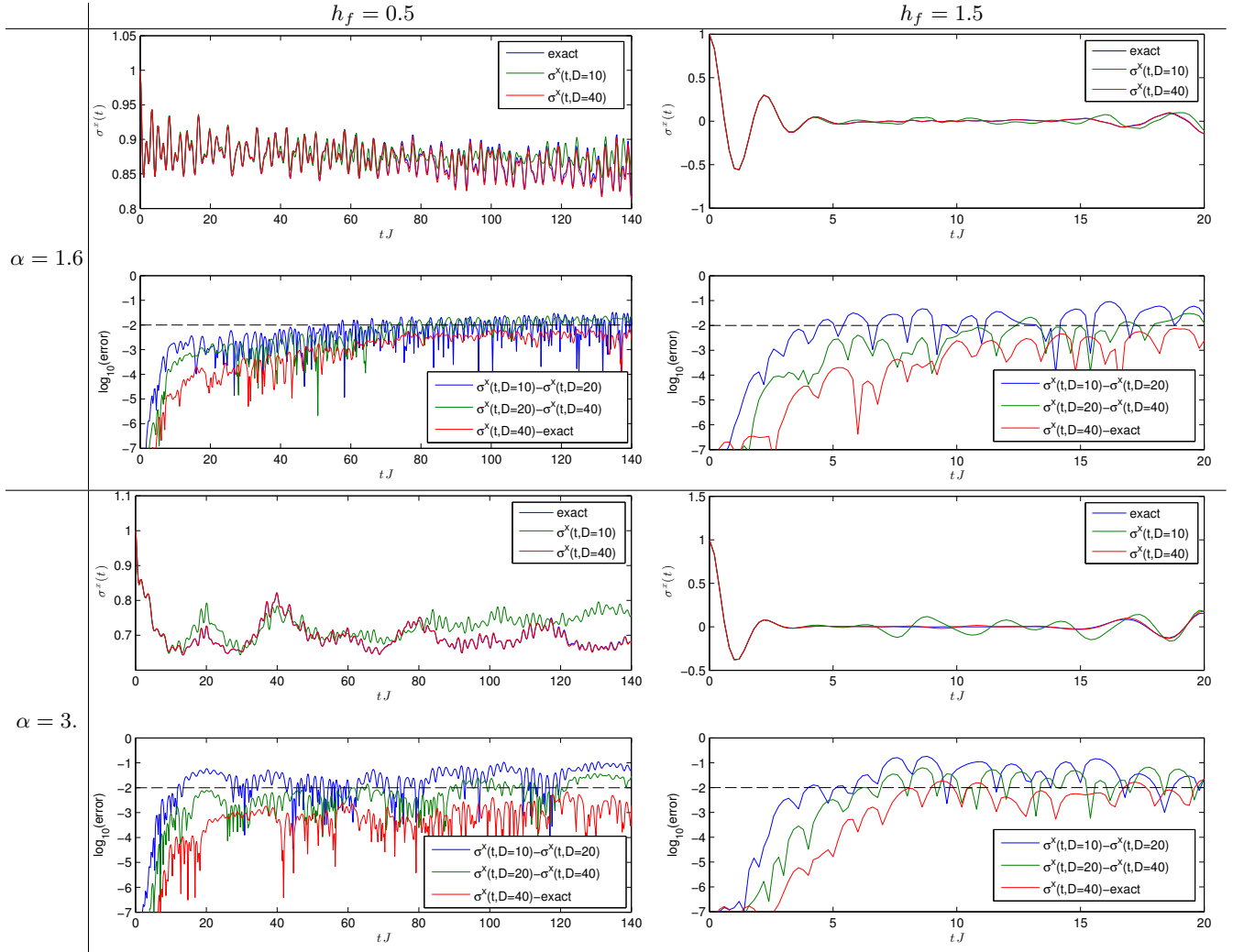


Figure 9: Comparison of the TDVP calculations of the time evolution of the order parameter $\sigma^x(t)$ with the exact results obtained by the Lanczos method. In the rows and columns we change α and h as indicated. We find that the error, calculated from the difference of the observables obtained for bond dimensions that differ by a factor of 2 is typically an order of magnitude smaller than the actual error.

III. METHODS

We use the time dependent variational principle (TDVP) applied to matrix product states described in [11,12](#), with the one-site second order integration method with step size 0.02, to simulate the dynamics of our model. Furthermore, we used a Hamiltonian matrix product operator description with a relative error smaller than 10^{-9} . In order to check convergence of the data we used increasing bond dimension for the variational Ansatz of the state. The largest bond dimension, for which the data in the main text is presented, is $D = 100$. In Figure 8 we compare the expectation values of $\sigma^x(t)$ for different h_f and $\alpha = 1.8, 2.5$ calculated for the bond dimensions $D = 60, 100$.

The phase diagram shown in the main text is calculated from the data averaged over a window of $tJ = 5$ around the "large" minimum before the revival (clearly seen for $\alpha = 2.5$) for $h_f < 1$ and around the latest converged window of size $tJ = 5$ for $h_f > 1$. In order to further justify our choice of times for which we compute the time-averaged order parameter, we compare the results of our method to exact diagonalization for small systems $N = 18$. In Figure 9 we show the time evolution of $\sigma^x(t)$ along with the errors. We compare the difference of the data calculated with bond dimensions that differ by a factor of two with the actual error and find that it is almost always around an order of magnitude smaller than the estimate. Besides, in the flat region where we extract the time average, the error does not grow significantly above 0.01, as the simulated curve does not start to deviate but rather oscillates around the exact value which further supports the robustness of our results.

Finally, we check the convergence of the Loschmidt echo and the return probability rates. In Figure 10 we show

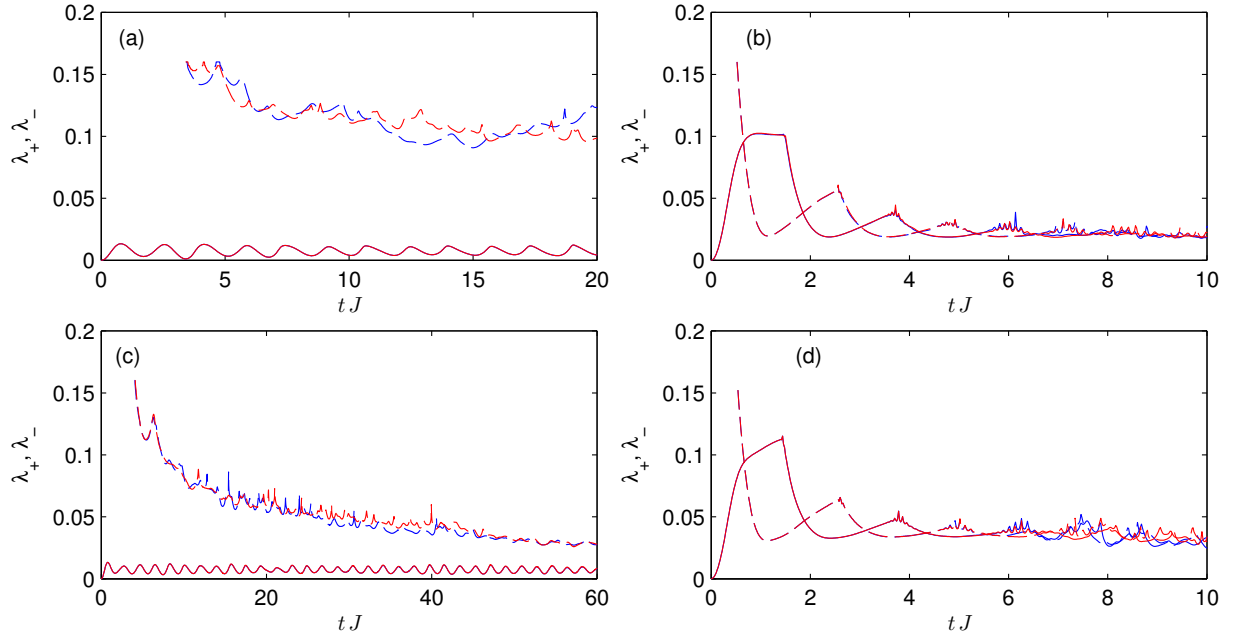


Figure 10: Convergence of the probabilities to return to the symmetry-broken ground states of the pre-quench Hamiltonian (denoted by dashed and full lines, respectively). We show data for $h = 0.5$ (a,c) and $h = 1.5$ (b,d) for interaction ranges $\alpha = 1.8$ (a,b) and $\alpha = 2.5$ (c,d). The color denotes different bond dimensions $D = 60$ (blue) and $D = 100$ (red).

the data for different quenches and ranges of interaction. For the considered time ranges the data has converged with the bond dimension.

-
- ¹ B. Sciolla and G. Biroli, J. Stat. Mech.: Theor. and Exper. **11**, P11003 (2011), URL <https://doi.org/10.1088/1742-5468/2011/11/P11003>.
 - ² B. Žunkovič, A. Silva, and M. Fabrizio, Philosophical Transactions of the Royal Society A: Mathematical, Physical and Engineering Sciences **374**, 20150160 (2016), URL <https://doi.org/10.1098/rsta.2015.0160>.
 - ³ M. Heyl, A. Polkovnikov, and S. Kehrein, Phys. Rev. Lett. **110**, 135704 (2013), URL <https://link.aps.org/doi/10.1103/PhysRevLett.110.135704>.
 - ⁴ M. Heyl, Phys. Rev. Lett. **113**, 205701 (2014), URL <https://link.aps.org/doi/10.1103/PhysRevLett.113.205701>.
 - ⁵ J. C. Halimeh and V. Zauner-Stauber, Phys. Rev. B **96**, 134427 (2017), URL <https://link.aps.org/doi/10.1103/PhysRevB.96.134427>.
 - ⁶ I. Homrighausen, N. O. Abeling, V. Zauner-Stauber, and J. C. Halimeh, Phys. Rev. B **96**, 104436 (2017), URL <https://link.aps.org/doi/10.1103/PhysRevB.96.104436>.
 - ⁷ V. Zauner-Stauber and J. C. Halimeh, Phys. Rev. E **96**, 062118 (2017), URL <https://link.aps.org/doi/10.1103/PhysRevE.96.062118>.
 - ⁸ J. C. Halimeh, V. Zauner-Stauber, I. P. McCulloch, I. de Vega, U. Schollwöck, and M. Kastner, Phys. Rev. B **95**, 024302 (2017), URL <https://link.aps.org/doi/10.1103/PhysRevB.95.024302>.
 - ⁹ P. Calabrese, F. H. L. Essler, and M. Fagotti, Phys. Rev. Lett. **106**, 227203 (2011), URL <https://link.aps.org/doi/10.1103/PhysRevLett.106.227203>.
 - ¹⁰ M. Kollar, F. A. Wolf, and M. Eckstein, Phys. Rev. B **84**, 054304 (2011), URL <https://link.aps.org/doi/10.1103/PhysRevB.84.054304>.
 - ¹¹ J. Haegeman, C. Lubich, I. Oseledets, B. Vandereycken, and F. Verstraete, Phys. Rev. B **94**, 165116 (2016), URL <https://link.aps.org/doi/10.1103/PhysRevB.94.165116>.
 - ¹² J. Haegeman, J. I. Cirac, T. J. Osborne, I. Pižorn, H. Verschelde, and F. Verstraete, Phys. Rev. Lett. **107**, 070601 (2011), URL <https://link.aps.org/doi/10.1103/PhysRevLett.107.070601>.